More than 40 years of potentially induced seismicity close to the San Andreas fault in San Ardo, central California

Thomas H. W. Goebel
Center for Earthquake Research and Information
University of Memphis, Tennessee, USA
thgoebel@memphis.edu

Manoochehr Shirzaei
Department of Geoscience
Virginia Tech, Blacksburg, VA, USA

September 26, 2020

1 Abstract

Evidence for fluid injection-induced seismicity is rare in California hydrocarbon basins, despite widespread injection close to seismically active faults. We investigate a potential case of injection-induced earthquakes associated with San Ardo oilfield operations which began in the early 50's. The largest potentially induced events occurred in 1955 (M_L5.2) and 1985 (M_w4.5) within $\sim$6 km from the oilfield. We analyze SAR interferometric images acquired by Sentinel-1A/B satellites between 2016 and 2020, and find surface deformation of up to 1.5 cm/yr, indicating pressure-imbalance in parts of the oilfield. Fluid-injection in San Ardo is concentrated within highly-permeable rocks directly above the granitic basement at depth of $\sim$800 m. Seismicity predominantly occurs along basement-faults at 6 to 13 km depths. Seismicity and wastewater disposal wells are spatially-correlated to the north of the oilfield. Temporal correlations are observed over more than 40 years with correlation coefficients up to 0.71 for seismicity within 24 km distance from the oilfield. Such large distances have not previously been observed in California but are similar to the large spatial footprint of injection in Oklahoma. The San Ardo seismicity shows anomalous clustering with earthquakes consistently occurring at close spatial-proximity but long inter-event times. Similar clustering has previously been reported in California geothermal fields and may be indicative of seismicity due to long-term, spatially-persistent external forcing.

The complexity of seismic behavior at San Ardo suggests that multiple processes, such as elastic stress transfer and aseismic slip transients, contribute to the potentially induced earthquakes. The present observations show that fluid-injection operations occur close to seismically-active faults in California. Yet, seismicity is predominantly observed on smaller unmapped faults with little observational evidence that large faults are sensitive to induced stress changes.

Keywords

induced seismicity, fluid injection, surface uplift, poroelastic stress, central California, San Ardo oilfield

2 Introduction

California's hydrocarbon basins contribute significantly to oil and gas production in the U.S. In 2015, the hydrocarbon industry in California involved 368,000 jobs and $111 billion in economic output, making California the 4th largest oil producing state (*Sedgwick and Mitra*, 2017). Previous studies suggest that past oil production in California have led to induced earthquakes, dating as far back as 1947 and as recently as the 1987 (M_w5.9) Whittier Narrows event (*Hough and Bilham*, 2018; *Hough et al.*, 2017; *Kovach*, 1974; *McGarr*, 1991). More recently, enhanced oil recovery techniques and wastewater disposal led to a surge of seismic activity in the central U.S. and Canada (e.g. *Atkinson et al.*, 2016; *Bao and Eaton*, 2016; *Ellsworth*, 2013; *Keranen et al.*, 2013). Such a surge is absent in California, although isolated induced cases have been reported due to water flooding, hydraulic fracturing and wastewater disposal (*Goebel et al.*, 2015; *Kanamori and Hauksson*, 1992; *Teng et al.*, 1973). The most recent example was an earthquake swarm with events up to M_w4.7 along the White-Wolf fault in 2005 (*Goebel et al.*, 2016). Thus, in spite of the long history of using enhanced oil recovery techniques in California, the seismogenic impact has been modest (at least after $\sim$1980) and is strikingly different from the recent wave of induced earthquakes e.g. in Texas and Oklahoma (*Göbel*, 2015; *Hauksson et al.*, 2015; *Skoumal et al.*, 2020; *Weingarten et al.*, 2015).

The apparent lack of conspicuous induced events in California compared to the central U.S. is surprising in light of the close spatial proximity of oilfield operations and seismically active faults. While operational parameters (i.e. injection rates and pressures) are comparable between California and the central U.S. (*Göbel*, 2015), other factors may explain the lack of induced events. Examples of such factors are: 1) ambient stresses, 2) local geology (e.g. distance to basement, hydrological structure, pressure compartmentalization) and 3) difficulty in differentiating induced and natural earthquake clusters. The latter is a key issue in regions with high background seismicity rates. Induced event detection is further inhibited because induced events may occur at more than 30 km from wells (*Keranen et al.*, 2014).

Many previous studies focused on near-well seismicity and fluid pressure effects as primary mechanism for induced earthquakes (*Healy et al.*, 1968; *Hsieh and Bredehoeft*, 1981; *Raleigh et al.*, 1976; *Shapiro et al.*, 1997; *Shirzaei et al.*, 2016). However, more recent observations highlight the importance of additional processes such as (poro)elastic stress changes which may be most pronounced at sedimentary injection sites right above the crystalline basement (e.g. *Barbour et al.*, 2017; *Chang and Segall*, 2016; *Goebel and Brodsky*, 2018; *Segall and Lu*, 2015; *Zhai et al.*, 2019). Additional sources of elastic stress include, for example, Coulomb stress changes from preceding ruptures as well as induced aseismic slip (*Bourouis and Bernard*, 2007; *Duboeuf et al.*, 2017; *Guglielmi et al.*, 2015; *Sumy et al.*, 2014).

Here, we focus on long-term seismic and oilfield records in San Ardo, central California, about 35 km west of the Parkfield segment of the San Andreas fault. The region is well-instrumented and hosts some of the largest wastewater disposal wells in California. We perform a detailed investigation of potentially induced seismicity north and northwest of San Ardo. We first investigate spatial correlations between injection and earthquakes and analyze the historic record of seismicity during the start of oilfield operations. We then examine the local geologic and surface deformation data, and inspect potential temporal correlations between injection and seismicity rates. Lastly, we discuss seismicity clustering characteristics and underlying mechanisms of the observed earthquakes in light of spatial seismicity decay and space-time migration.

3 Method and Data

Seismic and hydrological data

Monthly and annual injection and production data are publicly available from the California Division of Oil, Gas and Geothermal Resources (DOGGR). We analyzed both monthly injection and production data for each well and for the entire oilfield. These data are archived with some time lag and are presently available between 1977 and 2017. In addition, we extracted the depth interval of injections and geologic information from PDF-documents available through DOGGR.

Seismic data, including waveform records, phase data and earthquake catalogs, were obtained from the Northern California Earthquake Data Center (*NCEDC*, 2014). We analyzed both the standard catalogs that can directly be downloaded and created an improved catalog by joint event relocation. For this purpose, we first relocated all events with sufficient phase picks between 1970 and 2020 using a local velocity model (*Waldhauser et al.*, 2004) and the *NonLinLoc* program (*Lomax et al.*, 2009). We then relocated event clusters based on relative travel-time differences. No waveform data are available before 1984, phase picks are sparse, and location uncertainty, especially focal depths, are expected to be high (see below for details about uncertainty estimates). Waveform and phase data became available for 27 stations within 30 km and 72 stations within 50 km in 1984. We inspected the quality of waveform records and limit the analysis to phase picks with high signal-to-noise within 30 km. We find that using an automated AIC (Akaike-Information-Criterion) picker slightly improves phase picks compared to standard NCEDC picks. We recomputed absolute locations and then determined relative locations from event cross-correlations and differential travel times of clustered events using *GrowClust* (*Trugman and Shearer*, 2017). The combined catalog that includes all relocated events from these different approaches is plotted in Fig. 1. Events that formed clusters and were relocated with *GrowClust* are shown in the online supplement (Fig. S3).

The magnitude of completeness, M_c, for each catalog was determined by fitting magnitude distributions with the Gutenberg-Richter relationship and determining the magnitude cut-off that minimizes the misfit between the exponential fit and observed distribution (*Clauset et al.*, 2009). We determine a value of $M_c = 1.6$ (Fig. S4).

Geodetic analysis

We analyzed surface deformation across the San Ardo oilfield using a multi-temporal SAR interferometric analysis (*Shirzaei*, 2013). The analysis integrates a set of 101 SAR images acquired by the Sentinel-1A/B C-band satellites during November 2015 and January 2020 in descending frame 472 and path 42 (heading $\sim$193.1°and incidence $\sim$33.9°). We co-registered single look complex (SLC) images to a reference image, using a standard matching algorithm and subsequently enhanced spectral diversity (ESD) (*Shirzaei et al.*, 2017). We applied a multi-looking factor of 32 and 6 in range and azimuth, respectively, to obtain SLC images with pixel dimensions of $\sim 75\times75$ m. Using this dataset, we generated 404 high-quality interferograms (Fig. S5). We flattened each interferogram and removed the topographic phase using the Shuttle Radar Topography Mission DEM and precise satellite orbital information (*Farr et al.*, 2007). We identified high-quality pixels by performing a statistical test on the time series of complex interferometric phase noise which was estimated by wavelet multi-resolution analysis (*Shirzaei*, 2013). Next, we applied sparse phase unwrapping using a Minimum Cost Flow (MCF) algorithm to obtain absolute phase changes (*Costantini*, 1998). To correct for the spatially uncorrelated atmospheric delay, we applied a filter based on 2D wavelet multi-resolution. We solved for the surface deformation time-series using weighted least squares (*Shirzaei*, 2013). Lastly, we reduced residual atmospheric errors by applying a high-pass filter to the time series of each pixel (*Shirzaei*, 2013) and computed long-term displacement rates by fitting a slope to the deformation time-series.

4 Results

Seismicity along the Salinas basin and in the area between the San Andreas and Rinconada faults is generally sparse except for earthquake clusters close to San Ardo (Fig. 1 & S1). Here, seismic activity is concentrated north and northwest of the San Ardo oilfield. The most notable feature is a roughly linear earthquake cluster that extends from the oilfield boundary about 6 km north and includes four events above $M4$ since 1970 (Fig. 1 & S3). The latest $M>4$ event occurred on an unmapped fault in 1985 and was located roughly 6 km from the closest wastewater disposal well (Fig. 1).

Fluid-injection in the form of water flooding and steam injection occurs throughout the San Ardo oilfield. wastewater disposal, on the other hand, is concentrated to the north of the oilfield, with only few high-rate injectors to the east and south of the oilfield (Fig. 1). wastewater disposal wells in San Ardo operate at peak rates of more than 100,000 m^3/mo. The disposal wells in San Ardo are some of largest injectors in California hydrocarbon basins (99^{th} percentile) (*CA Department of Conservation*, 2012) and comparable to high-rate, earthquake-prone injectors within the central and eastern U.S. (*Weingarten et al.*, 2015).

Earthquakes and disposal wells are closely correlated at the surface, however they occur at substantially different depths. Much of the seismicity focuses at focal depths of 10 to 12 km (Fig. 1). Injection activity, on the other hand, is generally shallow between 500 to 880 m, with perforation zones slightly deepening toward the north. Average production depths are between 600 to 730 m (*CA Department of Conservation*, 2012). We observe one shallower seismicity cluster at 6 to 8 km depths within 2 km surface-distance from the injection wells and almost no seismicity above that. One deep cluster at $\sim$14 km depth is likely a result of insufficient station coverage and large event-station distances in the early 70's. This is reflected in vertical location uncertainties of up to 5.3 km (3 km horizontal) prior to $\sim$1980 and 2.6 km vertical and 1.2 km horizontal errors after 1984.

[Figure 1 about here.]

Instrumental earthquake records for San Ardo extend back to 1930, allowing us to examine seismic activity at the onset of oilfield operations. San Ardo is one of the most recently discovered oilfields in California. The first well was drilled in 1947 but pervasive production and injection did not start until

1952 according to DOGGR records. The historic seismicity records include only three events between 1930 and 1952 when operations started (Fig. 2). The onset of operations is followed by an increase in seismic activity within ∼8 km from the oilfield including a M_L5.2 event in 1955 and three M>4 events in the mid 70's. This increase in seismic activity is not simply due to changes in station density because the number of stations in the area remained roughly constant until 1966 (pers. comm. Stephane Zuzlewski, UC Berkeley, Dave Oppenheimer, USGS). It should be noted that one M5 event in 1932 was erroneously located close to San Ardo in some earlier earthquake catalogs (e.g. *Poley*, 1988). This event has since been relocated closer towards Point Sur in agreement with felt shaking effects (*Toppozada et al.*, 2002) and is hence not considered within this study.

[Figure 2 about here.]

More recent records from 1977 to 2017 highlight that oil production in San Ardo is correlated with oil price variations, similar to other regions in California (*Göbel*, 2015). Elevated prices and oilfield activity are observed until the mid-'80s followed by low activity throughout the 90's and steady increase in price and produced oil until 2015 (Fig. S7). Wastewater disposal volumes were high until the mid-'80s and showed a short period of low volumes between 1989 and 1995, followed by a steady increase until 2003 when disposal-volumes plateaued.

4.1 Geology and surface deformation

Oil production in San Ardo takes advantage of relatively shallow oil-sands east of the Hamas Valley Trough which is located at the eastern flank of the Rinconada fault (Fig. 3). The oil sand formations are located directly above the granitic basement at depths of less than 1 km. The upper basement appears to host many fractures and faults based on seismic reflection imaging, however the extent and orientation of upper basement faulting is largely unknown (*Menotti*, 2014). wastewater disposal is concentrated in the north of

San Ardo either in high-permeability oil-sands (k = 2-8 $\cdot 10^{-12}$ m^2, porosity=23-39%) or directly within the fractured upper basement (*CA Department of Conservation*, 2012) (Fig. 3).

[Figure 3 about here.]

The relatively shallow injection activity is associated with surface uplift across the oilfield. This uplift was first resolved in independent studies which focused on the neighboring creeping segment of the San Andreas fault (*Donnellan et al.*, 2017; *Jolivet et al.*, 2015; *Khoshmanesh and Shirzaei*, 2018). We further explore the effect of fluid injections on surface deformation, using long-term InSAR deformation rate between 2016 and 2020 (Fig. 4 & S6). Our results resolve peak line-of-sight (LOS) displacement rates of the imaging satellite of $\sim$1.5 cm/yr. Displacements are highest in an area that is surrounded by many high-rate injection wells. Cumulative LOS displacements were $\sim$5 cm between 2016 and 2020. We validate the InSAR observations against GPS measurements, and determine a high accuracy of the velocity map with an overall standard deviation of $\sim$2.3 mm/yr of InSAR relative to GPS measurements (Fig. 4 B).

The observed deformation is an expression of pervasive fluid injection activity and provides a direct indication of a poroelastic response associated with reservoir pressure increase. The largest displacements appear shifted from the highest-rate wastewater disposal wells. This spatial shift is similar to observations in east Texas, indicating that poroelastic deformation occurs where rocks are most compliant (*Shirzaei et al.*, 2016).

[Figure 4 about here.]

4.2 Temporal correlation of seismicity and injection rates

We inspect temporal correlations between injection/production and seismicity rates in San Ardo. Wastewater disposal and seismicity rates appear correlated within certain time periods such as during a pronounced minimum in the early 90's, followed by a strong rate increase until $\sim$2003 (Fig. 5). To avoid introducing biases from aftershock clustering in our analysis, we remove aftershocks within a fixed space-time window based on mainshock magnitude (*Gardner and Knopoff*, 1974). This declustering removes e.g. a local peak associated with the $M4.5$ event in 1985. We compare the results from fixed space-time declustering with a nearest-neighbor declustering method and find the catalogs to be identical except for 3 events. We examine the effects of regional, large-magnitude events ($M \geq 6$) i.e. the Coalinga, San Simeon and Parkfield events and find little associated change in seismicity rates in San Ardo (Fig. 5).

[Figure 5 about here.]

We test the robustness of the initial observations by performing a more systematic temporal analysis of seismicity and injection rates. For this purpose, we sample the earthquake data at increasing distances from 5 to 45 km and cross-correlate resulting seismicity and injection time series at peak lag-times of ± 40 month. We test the significance of resulting correlations by Monte Carlo resampling of catalogs with random Poissonian rates while conserving the original spatial and magnitude distributions. We find that correlations are not statistically significant at smaller distances (< 8 km) as a result of insufficient number of earthquakes. Beyond that distance, correlation coefficients increase from 0.35 at 9 km to 0.71 at 24 km distance (Fig. 6). At distances greater than 24 km, correlation coefficients start to decrease due to the inclusion of more San Andreas fault events. Lag-times increase gradually from 13 to 17 months for increasing distances from 9 to 24 km with seismicity following injection rate changes. Beyond 24 km, lag-times increase rapidly to more than 30 months. Wastewater disposal and seismicity rates are more strongly correlated than other operational parameters such as fluid production, water flooding and steam injection (Fig. S7).

[Figure 6 about here.]

The cross-correlation results highlight that seismicity and injection rates are strongly linked at large scales, i.e. at up to 24 km distance from the oilfield. This observation mirrors results from Oklahoma. We examine potential parallels between Oklahoma and San Ardo in more detail in the Discussion section.

4.3 Seismicity clustering characteristics

As an additional independent metric for potentially induced events, we analyze the space-time clustering of the local earthquakes compared to the overall seismicity in Northern California. We separate the record of earthquake locations, origin times and magnitudes into clustered and background events. This separation is based on nearest-neighbor event-pairs which are determined from inter-event distances and times scaled by parent event magnitude (*Zaliapin and Ben-Zion*, 2013). The observed nearest-neighbor distance distributions are compared with randomized Poissonian catalogs that have the same number of events and magnitude distributions as the original catalogs. The resulting times-distance distributions can be categorized into clustered events (i.e. aftershocks) at times and distances below the 99^{th} percentile of the randomized catalogs (gray dashed line in Fig. 7), and background at large distance. To avoid biases due to different location procedures we use the standard NCEDC catalog for the analysis of earthquake clustering.

We find notable differences in clustering characteristics between the overall Northern California catalog and the local San Ardo events. For the Northern California seismicity, we observe two statistical modes separated by a gray dashed line in Fig. 7. These modes highlight background events at large and aftershocks at small space-time distances. The San Ardo seismicity differs from this behavior. The overall density map is shifted to longer inter-event times due to comparably lower rates. The clustered mode is still present at roughly the same rescaled distances ($\log R = -2.4$ to -1) but much less significant than for the whole catalog. An additional mode is visible below the clustered event mode at larger inter-event times but small distances. This mode is labeled *Induced* in Fig. 7 based on earlier results of induced event detection in geothermal reservoirs (*Zaliapin and Ben-Zion*, 2016). The induced events are essentially occurring at the same location but distributed over long-periods, which could be indicative of persistent external forcing in the area. The overall seismicity clustering characteristics in San Ardo are consistent for magnitudes of completeness between 1 and 2.

We assess whether the induced $R - \tau$ mode in San Ardo is uncommon for Northern California by examining 1D conditional distributions of inter-event times, τ at small distances R (i.e. $\log R \leq -2.5$). We compare the observed conditional distribution for San Ardo with 1000 Monte-Carlo resampled earthquake catalogs and assess differences in the distribution using a 2-sample KS-statistic. This test yields a significance level of p=0.92 for the third mode observed in San Ardo or in other words 8% of the sub-catalogs show similar characteristics to San Ardo at small distances. The result indicates that the observations in San Ardo are uncommon but not unique, i.e. other areas show similar characteristics of spatial clustering over long periods. Such clustering is expected in areas with pervasive induced and natural swarm activity such as the Geysers north of San Francisco and the Long Valley Caldera in eastern California. The induced mode together with the more dominant background mode in San Ardo are in line with space-time-magnitude clustering of induced events in geothermal reservoirs and may be a useful first indicator of the presence of induced seismicity.

[Figure 7 about here.]

5 Discussion

Several observations indicate that the San Ardo earthquakes are induced while others support a tectonic origin of the events. For instance, the depth separation between injection wells and earthquakes between 4 and 10 km is large and exceeds observations in other places. Previously, large focal depths were thought to preclude an induced origin of seismic events (e.g. *Davis and Frohlich*, 1993). However more recent observations highlight that large volume, low pressure fluid disposal operations can lead to seismicity at large distances and depths (*Chen et al.*, 2018; *Goebel et al.*, 2017a; *Keranen et al.*, 2014; *Schoenball and Ellsworth*, 2017). Tectonic seismicity-clusters occur throughout California and are not always bound to mapped faults. The

San Ardo seismicity may be no exception. Nevertheless, several observations suggest a link between oil-field operations and the earthquakes.

We observe both strong temporal and spatial correlation between seismicity and wastewater disposal in the northern part of the oilfield. Injection occurs in close proximity to the granitic basement which has been identified as a particularly problematic depth for injection operations (*Goebel and Brodsky*, 2018; *Hincks et al.*, 2018; *Horton*, 2012; *Skoumal et al.*, 2018). The injection rates in San Ardo are high, comparable to seismogenic injection in the central U.S.. High-volume and high-rate injectors are expected to increase the probability of measurable seismogenic effects (*McGarr*, 2014; *Weingarten et al.*, 2015). Lastly, the seismicity clustering in space and time is comparable to observations of induced events in geothermal fields (*Schoenball et al.*, 2015; *Zaliapin and Ben-Zion*, 2016). Such clustering is particularly interesting because it may provide a way to detect induced sequences without any knowledge of oilfield operations.

Induced seismicity in California is difficult to detect outside of geothermal reservoirs. We show that the combination of long-term seismic, hydrological and geodetic records can be useful in evaluating potentially induced events. Previous studies in California hydrocarbon basins mainly reported subsidence due to production (e.g. *Jolivet et al.*, 2015; *Kovach*, 1974), whereas we present novel observations of significant surface uplift. This highlights that fluid volumes are not always balanced, leading to increasing reservoir pressure and poroelastic expansion.

5.1 Comparing induced seismicity in San Ardo and Oklahoma

The here observed seismicity and injection characteristics show several similarities to observations in Oklahoma: 1) For both Oklahoma and San Ardo, injection rates seem to be best correlated with seismicity at large distances, i.e. out to $\sim$24 km in San Ardo and $>$30 km in Oklahoma. In Oklahoma, recent results highlight that injection and seismicity rates are strongly correlated at basin-wide scales (*Langenbruch and*

Zoback, 2016; *Zhai et al.*, 2019). These correlations deteriorate quickly at the scale of individual sequences. A possible explanation for this observation is that local crustal heterogeneity controls earthquake rates at small scales whereas the large-scale response is controlled by external forcing, i.e. induced stress and injection rates.

2) We observed a significant time-lag of 13 to 17 months between injection and seismicity rates which is comparable to time-lags of 10 to 21 months for large-scale correlations in Oklahoma (*Chen et al.*, 2017; *Goebel et al.*, 2017b; *Zhai et al.*, 2019).

3) Injection may occur much shallower than associated seismicity. For example, the Pawnee earthquakes in 2016 were linked to injection between 1300 and 1900 m while seismic activity occurred between 5 to 7 km depths (*Barbour et al.*, 2017; *Yeck et al.*, 2017).

4) Injection operations include many high-rate wells that take advantage of high-permeability layers above the crystalline basement (*Hincks et al.*, 2018; *Keranen et al.*, 2014; *Weingarten et al.*, 2015).

The present study confirms that local geologic setting may be a key driver in elevating induced seismic hazard (*Hincks et al.*, 2018; *Skoumal et al.*, 2018). Based on this result, we suggest that the deep sedimentary basin within the Central Valley, CA could be a safer place for injecting wastewater than San Ardo. This may be similar for other deep basins such as Ventura basin, however more studies are needed to assess induced seismic hazards.

5.2 Physical mechanisms for the potentially induced earthquakes

One particularly unexpected observation in San Ardo is the large vertical separation between injection and earthquakes, which is hard to reconcile with fluid pressure diffusion and effective stress reduction. As a consequence, a combination of mechanisms is required to explain the potentially induced origin of the earthquakes.

One such explanation is that fault damage zones can act as flow conduits which facilitate pressure diffusion to large depths (*Goebel et al.*, 2016; *Hornbach et al.*, 2015; *Ogwari and Horton*, 2016; *Zhang et al.*, 2013). This mechanism hinges on wide-spread hydraulic connectivity and consistently-high fault permeability from the point of injection to seismogenic depths.

Other explanations include the effect of elastic stress transfer processes. The observed surface uplift supports a poroelastic expansion of the reservoir which would create elastic stresses that decay as a power-law outside of the oilfield (*Goebel et al.*, 2017a; *Helm*, 1994; *Segall and Lu*, 2015; *Wang*, 2000). Elastic stresses are a result of pore pressure increase at undrained conditions, leading to fault activation even without direct hydraulic connectivity (*Wang*, 2000). The seismicity in San Ardo shows a power-law spatial decay between 2 to 20 km with an exponent of $\sim r^{-1.8}$ (Fig. 8). The same power-law exponent has been observed for induced seismicity associated with isolated injection wells (*Goebel and Brodsky*, 2018).

[Figure 8 about here.]

In addition, elastic stress transfer from aseismic processes may contribute to the observed seismicity (*Guglielmi et al.*, 2015). This is supported by intermittent linear space-time migration at distances of 1 to 6 km from the wells (Fig. 9). Near-well regions within ∼1.5 km from the oilfield are largely aseismic with few seismic episodes. Beyond this zone, seismicity sequences form 1.5 to 4 km long linear streaks with migration velocities between 20 m/dy and 1 km/dy (black arrows in Fig. 9). Migration velocity at other sites with injection induced seismicity, such as Paralana, Soultz, St. Gallen, Basel and Paradox Valley fall within a similar range of meters to hundreds of meters/day (*Bourouis and Bernard*, 2007; *Goebel and Brodsky*, 2018; *Kraft and Deichmann*, 2014). Aseismic slip during shallow controlled injection experiments can even be one order of magnitude slower (*Guglielmi et al.*, 2015). The observed linear clusters are markedly different from classic square-root migration associated with diffusive processes (*Shapiro et al.*, 1997).

[Figure 9 about here.]

While higher pore pressure generally moves faults closer to failure, resulting fault-slip may not always be seismic. Previous controlled injection tests confirm that high fluid pressures favor stable sliding over unstable stick-slip (*Cappa et al.*, 2019; *Guglielmi et al.*, 2015). In these experiments, fault slip within the pressurized region close to injection-wells did not produce seismic events due to rate-strengthening effects and increase of critical fault stiffness due to higher pore pressures (*Cappa et al.*, 2019; *Scuderi and Collettini*, 2016). Observations in San Ardo provide some support for this model, i.e. predominantly aseismic behavior within 1.5 km from the oilfield followed by linear seismicity migration at larger distance either due to elastic stresses or seismic asperities (*Bourouis and Bernard*, 2007).

5.3 Different classes of induced seismicity

Not all induced earthquake sequences are equal and respective differences in space-time-magnitude characteristics support a classification into different groups of induced events. We differentiate two end-member groups:

1) Induced events that occur in tight clusters around injection wells which operate at high pressures within low permeability formations e.g. within the crystalline basement or tight shales. Such operations may include hydraulic stimulation (e.g. hydro-shearing and hydraulic fracturing) with rapid onset and arrest of seismicity sequences (e.g. *Brown et al.*, 2012; *Dempsey et al.*, 2016; *Raleigh et al.*, 1976; *Shapiro et al.*, 1997, 2006). Compact induced seismicity clusters commonly show high Gutenberg-Richter *b*-values, pronounced square-root migration patterns and rapid spatial decay (*Eaton et al.*, 2014; *Goebel and Brodsky*, 2018; *Maxwell et al.*, 2009). Aftershock productivity and triggering potential is generally lower than for natural earthquakes (*Maghsoudi et al.*, 2018; *Zaliapin and Ben-Zion*, 2016). The expected maximum magnitude of events is closely related to the size of the stimulated reservoir (*Eaton et al.*, 2014; *Shapiro et al.*, 2011).

2) Spatially extensive induced clusters at large distances and depths from wells can occur many months

after injection operations (*Ogwari et al.*, 2018). Such seismic events are typically associated with high-volume, low-pressure wastewater disposal in permeable reservoirs, located directly above the crystalline basement (*Hincks et al.*, 2018; *Skoumal et al.*, 2018). The induced events show power law spatial decay from injection wells, and *b*-values close to or even below unity (*Goebel et al.*, 2016; *Huang and Beroza*, 2015; *Skoumal et al.*, 2014). Aftershock productivity may be higher than for tectonic events (*Goebel et al.*, 2019; *Llenos and Michael*, 2013). The presence of far-reaching elastic effects suggests that the maximum magnitude is only limited by the regional tectonic maximum event size (*van der Elst et al.*, 2016).

In principle, the differences in seismicity statistics of unfolding induced earthquake sequences allow for a separation into these two different groups. However, transitions between group 1) and 2) are expected e.g. for multi-stage lateral hydraulic fracturing and accidental activation of a near-by fault (*Igonin et al.*, 2018; *Kim et al.*, 2018; *Maxwell et al.*, 2009). Such transitions can complicate an exact classification of induced sequences in some cases or at least require extensive, high-resolution seismic records. When possible, distinguishing groups 1) and 2) based on dominant seismicity characteristics will improve the understanding of underlying physics and associated seismic hazard.

6 Conclusion

Detailed analysis of more than 40 years of high-resolution seismic data in close proximity to San Ardo oil-field, central California, indicates a potential connection between wastewater disposal and seismic activity. The seismicity shows significant spatial-temporal correlations with fluid injection. Temporal correlations are strongest for events within 24 km from the disposal wells which is also the distance to the near-by San Andreas fault. We find that seismicity clustering, specifically at small inter-event distance but long inter-event time, is anomalous compared to average behavior in Northern California. Similar clustering characteristics have been observed for induced events in geothermal reservoirs. Criteria that elevate injection-induced seismic hazard in California and elsewhere are: 1) Injection directly above basement, 2) high-rate, broad-scale injection into permeable zones, and 3) the presence of tectonically-stressed faults. These criteria may help guide future fluid-injection operations.

While California does not exhibit as many induced earthquakes as the central U.S., the state allows for high-resolution long-term studies which can help mitigate induced seismic hazards by resolving the underlying physical processes. Several factors may have contributed to the earthquakes near San Ardo. The observed spatial seismicity decay approximately matches power-law elastic stress decay outside of a pressurized reservoir. In addition, linear seismicity migration may indicate aseismic slip transients, associated with episodic earthquakes at seismic asperities.

Data and Resources

Sentinel-1 SAR data were obtained through Alaska Satellite Facilities (asf.alaska.edu). GPS data are obtained from Nevada Geodetic Laboratory (http://geodesy.unr.edu/). Waveform data, metadata, or data products for this study were accessed through the Northern California Earthquake Data Center (NCEDC), doi:10.7932/NCEDC. Oilfield operational data for California is archived by DOGGR (secure.conservation.ca.gov/WellSearch). The online supplement of this article includes an animation of seismicity and injection operations as well as a PDF document with additional figures of seismicity, oilfield operations and surface velocities.

Acknowledgments

The authors would like to thank Stephane Zuzlewski, Dave Oppenheimer, Dave Shelly, Emily Brodsky, Ilya Zaliapin and Joern Davidsen for discussions. Mitch Withers and Charles Langston provided helpful comments on an earlier version of the manuscript. The manuscript benefited from reviews by Art McGarr and Gillian Foulger. We acknowledge Pranav Appani for his help in compiling operational data from the California Division of Oil, Gas and Geothermal Resources. This research was supported by Department of Energy grant DE-SC0015539 to TG and grant DE-SC0019307 to MS.

References

Atkinson, G. M., D. W. Eaton, H. Ghofrani, D. Walker, B. Cheadle, R. Schultz, R. Shcherbakov, K. Tiampo, J. Gu, R. M. Harrington, Y. Liu, M. van der Baan, and H. Kao, Hydraulic Fracturing and Seismicity in the Western Canada Sedimentary Basin, *Seismological Research Letters*, *87*, 631–647, 2016.

Bao, X., and D. W. Eaton, Fault activation by hydraulic fracturing in western Canada, *Science*, *354*, 1406–1409, 2016.

Barbour, A. J., J. H. Norbeck, and J. L. Rubinstein, The Effects of Varying Injection Rates in Osage County, Oklahoma, on the 2016 M w 5.8 Pawnee Earthquake, *Seismological Research Letters*, *88*, 1040–1053, 2017.

Bourouis, S., and P. Bernard, Evidence for coupled seismic and aseismic fault slip during water injection in the geothermal site of Soultz (France), and implications for seismogenic transients, *Geophysical Journal International*, *169*, 723–732, 2007.

Brown, D. W., D. V. Duchane, G. Heiken, and V. T. Hriscu, *Mining the Earth's Heat: Hot Dry Rock Geothermal Energy*, Springer Berlin Heidelberg, Berlin, Heidelberg, 2012.

CA Department of Conservation, Division of {O}il, {G}as and {G}eothermal Resources: {P}roduction History in {C}alifornia, 2012.

Cappa, F., M. M. Scuderi, C. Collettini, Y. Guglielmi, and J.-P. Avouac, Stabilization of fault slip by fluid injection in the laboratory and in situ, *Science Advances*, *5*, eaau4065, 2019.

Chang, K. W., and P. Segall, Seismicity on Basement Faults Induced by Simultaneous Fluid Injection–Extraction, *Pure and Applied Geophysics*, *173*, 2621–2636, 2016.

Chen, X., N. Nakata, C. Pennington, J. Haffener, J. C. Chang, X. He, Z. Zhan, S. Ni, and J. I. Walter, The

Pawnee earthquake as a result of the interplay among injection, faults and foreshocks, *Scientific Reports*, *7*, 4945, 2017.

Chen, X., J. Haffener, T. H. W. Goebel, X. Meng, Z. Peng, and J. C. Chang, Temporal Correlation Between Seismic Moment and Injection Volume for an Induced Earthquake Sequence in Central Oklahoma, *Journal of Geophysical Research: Solid Earth*, *123*, 3047–3064, 2018.

Clauset, A., C. R. Shalizi, and M. E. J. Newmann, Power-law distributions in empirical data, *SIAM review*, *51*, 661–703, 2009.

Costantini, M., A novel phase unwrapping method based on network programming, *IEEE Transactions on Geoscience and Remote Sensing*, *36*, 813–821, 1998.

Davis, S. D., and C. Frohlich, Did (or will) fluid injection cause earthquakes?-criteria for a rational assessment, *Seismol. Res. Lett.*, *64*, 207–224, 1993.

Dempsey, D., C. Barton, and A. Catalinac, Density of induced earthquake hypocenters as a proxy for pore pressure increase during well stimulation, *50th US Rock Mechanics / Geomechanics Symposium*, *13-217*, 2016.

Donnellan, A., R. Arrowsmith, S. DeLong, A. Donnellan, R. Arrowsmith, and S. DeLong, Spatio-Temporal Mapping of Plate Boundary Faults in California Using Geodetic Imaging, *Geosciences*, *7*, 15, 2017.

Duboeuf, L., L. De Barros, F. Cappa, Y. Guglielmi, A. Deschamps, and S. Seguy, Aseismic Motions Drive a Sparse Seismicity During Fluid Injections Into a Fractured Zone in a Carbonate Reservoir, *Journal of Geophysical Research: Solid Earth*, *122*, 8285–8304, 2017.

Eaton, D. W., J. Davidsen, P. K. Pedersen, and N. Boroumand, Breakdown of the Gutenberg-Richter relation for microearthquakes induced by hydraulic fracturing: Influence of stratabound fractures, *Geophysical Prospecting*, *62*, 806–818, 2014.

Ellsworth, W. L., Injection-Induced Earthquakes, *Science*, *341*, 1225,942–1225,942, 2013.

Farr, T. G., P. A. Rosen, E. Caro, R. Crippen, R. Duren, S. Hensley, M. Kobrick, M. Paller, E. Rodriguez, L. Roth, D. Seal, S. Shaffer, J. Shimada, J. Umland, M. Werner, M. Oskin, D. Burbank, and D. Alsdorf, The Shuttle Radar Topography Mission, *Reviews of Geophysics*, *45*, RG2004, 2007.

Gardner, J. K., and L. Knopoff, Is the sequence of earthquakes in southern California, with aftershocks removed, Poissonian?, *Bull. Seismol. Soc. Am*, *64*, 1363–1367, 1974.

Göbel, T., A comparison of seismicity rates and fluid-injection operations in Oklahoma and California: Implications for crustal stresses, *The Leading Edge*, *34*, 640–648, 2015.

Goebel, T., M. Weingarten, X. Chen, J. Haffener, and E. Brodsky, The 2016 Mw5.1 Fairview, Oklahoma earthquakes: Evidence for long-range poroelastic triggering at >40 km from fluid disposal wells, *Earth and Planetary Science Letters*, *472*, 50–61, 2017a.

Goebel, T., Z. Rosson, E. Brodsky, and J. Walter, Aftershock deficiency of induced earthquake sequences during rapid mitigation efforts in Oklahoma, *Earth and Planetary Science Letters*, *522*, 135–143, 2019.

Goebel, T. H. W., and E. E. Brodsky, The spatial footprint of injection wells in a global compilation of induced earthquake sequences, *Science*, *361*, 899–904, 2018.

Goebel, T. H. W., E. Hauksson, F. Aminzadeh, and J. P. Ampuero, An objective method for the assessment of fluid injection-induced seismicity and application to tectonically active regions in central California, *Journal of Geophysical Research: Solid Earth*, 2015.

Goebel, T. H. W., S. M. Hosseini, F. Cappa, E. Hauksson, J. P. Ampuero, F. Aminzadeh, and J. B. Saleeby, Wastewater disposal and earthquake swarm activity at the southern end of the Central Valley, California, *Geophys. Res. Lett.*, *43*, 1–8, 2016.

Goebel, T. H. W., J. I. Walter, K. Murray, and E. E. Brodsky, Comment on "How will induced seismicity in Oklahoma respond to decreased saltwater injection rates?" by C. Langenbruch and M. D. Zoback, *Science Advances*, *3*, e1700,441, 2017b.

Guglielmi, Y., F. Cappa, J.-P. Avouac, P. Henry, and D. Elsworth, Seismicity triggered by fluid injection-induced aseismic slip, *Science*, *348*, 1224–1226, 2015.

Hauksson, E., T. Göbel, J.-p. Ampuero, and E. Cochran, A century of oil-field operations and earthquakes in the greater Los Angeles Basin , southern California, *The Leading Edge*, *34*, 650–656, 2015.

Healy, J. H., W. W. Rubey, D. T. Griggs, and C. B. Raleigh, The Denver Earthquakes, *Science*, *161*, 1301–1310, 1968.

Helm, D. C., Horizontal aquifer movement in a Theis-Thiem confined system, *Water Resources Research*, *30*, 953–964, 1994.

Hincks, T., W. Aspinall, R. Cooke, and T. Gernon, Oklahoma's induced seismicity strongly linked to wastewater injection depth, *Science*, *359*, 1251–1255, 2018.

Hornbach, M. J., H. R. DeShon, W. L. Ellsworth, B. W. Stump, C. Hayward, C. Frohlich, H. R. Oldham, J. E. Olson, M. B. Magnani, C. Brokaw, and J. H. Luetgert, Causal factors for seismicity near Azle, Texas, *Nature Communications*, *6*, 6728, 2015.

Horton, S., Disposal of Hydrofracking Waste Fluid by Injection into Subsurface Aquifers Triggers Earthquake Swarm in Central Arkansas with Potential for Damaging Earthquake, *Seismological Research Letters*, *83*, 250–260, 2012.

Hough, S. E., and R. Bilham, Poroelastic stress changes associated with primary oil production in the Los Angeles Basin, California, *The Leading Edge*, *37*, 108–116, 2018.

Hough, S. E., V. C. Tsai, R. Walker, and F. Aminzadeh, Was the Mw 7.5 1952 Kern County, California, earthquake induced (or triggered)?, *Journal of Seismology*, *21*, 1613–1621, 2017.

Hsieh, P. A., and J. D. Bredehoeft, A reservoir analysis of the Denver earthquakes: A case of induced seismicity, *Journal of Geophysical Research*, *86*, 903, 1981.

Huang, Y., and G. C. Beroza, Temporal variation in the magnitude-frequency distribution during the Guy-Greenbrier earthquake sequence, *Geophysical Research Letters*, *42*, 6639–6646, 2015.

Igonin, N., M. Zecevic, and D. W. Eaton, Bilinear Magnitude-Frequency Distributions and Characteristic Earthquakes During Hydraulic Fracturing, *Geophysical Research Letters*, *45*, 12,866–12,874, 2018.

Jolivet, R., M. Simons, P. S. Agram, Z. Duputel, and Z.-K. Shen, Aseismic slip and seismogenic coupling along the central San Andreas Fault, *Geophysical Research Letters*, *42*, 297–306, 2015.

Kanamori, H., and E. Hauksson, A slow earthquake in the Santa Maria Basin, California, *Bull. Seism. Soc. Am.*, *82*, 2087–2096, 1992.

Keranen, K., M. Weingarten, and G. Abers, Sharp increase in central Oklahoma seismicity since 2008 induced by massive wastewater injection, *Science*, *345*, 448–451, 2014.

Keranen, K. M., H. M. Savage, G. a. Abers, and E. S. Cochran, Potentially induced earthquakes in Oklahoma, USA: Links between wastewater injection and the 2011 Mw 5.7 earthquake sequence, *Geology*, *41*, 699–702, 2013.

Khoshmanesh, M., and M. Shirzaei, Episodic creep events on the San Andreas Fault caused by pore pressure variations, *Nature Geoscience*, *11*, 610–614, 2018.

Kim, K.-H., J.-H. Ree, Y. Kim, S. Kim, S. Y. Kang, and W. Seo, Assessing whether the 2017 M w 5.4 Pohang earthquake in South Korea was an induced event, *Science*, *360*, 1007–1009, 2018.

Kovach, R. L., Source Mechanisms for Wilmington Oil Field, California, Subsidence Earthquakes., *Bulletin of the Seismological Society of America*, *64*, 699–711, 1974.

Kraft, T., and N. Deichmann, High-precision relocation and focal mechanism of the injection-induced seismicity at the Basel EGS, *Geothermics*, *52*, 59–73, 2014.

Langenbruch, C., and M. D. Zoback, How will induced seismicity in Oklahoma respond to decreased saltwater injection rates?, *Science Advances*, *2*, 1–9, 2016.

Llenos, A. L., and A. J. Michael, Modeling earthquake rate changes in Oklahoma and Arkansas: Possible Signatures of induced seismicity, *Bulletin of the Seismological Society of America*, *103*, 2850–2861, 2013.

Lomax, a., a. Michelini, and a. Curtis, Earthquake location, direct, global-search methods, *Encyclopedia of Complexity and System Science*, pp. 2449–2473, 2009.

Maghsoudi, S., J. Baró, A. Kent, D. Eaton, and J. Davidsen, Interevent Triggering in Microseismicity Induced by Hydraulic Fracturing, *Bulletin of the Seismological Society of America*, *108*, 1133–1146, 2018.

Maxwell, S. C., M. Jones, R. Parker, S. Miong, S. Leaney, D. Dorval, D. D'Amico, J. Logel, E. Anderson, and K. Hammermaster, Fault activation during hydraulic fracturing, in *SEG Technical Program Expanded Abstracts 2009*, June 2010, pp. 1552–1556, Society of Exploration Geophysicists, 2009.

McGarr, A., Maximum magnitude earthquakes induced by fluid injection, *Journal of Geophysical Research: Solid Earth*, *119*, 1–12, 2014.

McGarr, A. F., On a possible connection between three major earthquakes in California and oil production, *Bulletin of the Seismological Society of America*, *81*, 948–970, 1991.

Menotti, T., Petroleum system evolution, strike-slip tectonism, and diagenesis of the Monterey formation in the Salinas basin, California, *Dissertation, Geological Sciences, Stanford University*, *01*, 304, 2014.

NCEDC, Northern California Earthquake Data Center. UC Berkeley Seismological Laboratory. Dataset, *NCEDC*, 2014.

Ogwari, P. O., and S. P. Horton, Numerical model of pore-pressure diffusion associated with the initiation of the 2010–2011 Guy–Greenbrier, Arkansas earthquakes, *Geofluids*, *16*, 954–970, 2016.

Ogwari, P. O., H. R. DeShon, and M. J. Hornbach, The Dallas-Fort Worth Airport Earthquake Sequence: Seismicity Beyond Injection Period, *Journal of Geophysical Research: Solid Earth*, 2018.

Poley, C. M., The San Ardo, California, earthquake of 24 November 1985, *Bull. Seis. Soc. Am.*, *78*, 1360–1366, 1988.

Raleigh, C. B., J. H. Healy, and J. D. Bredehoeft, An Experiment in Earthquake Control at Rangely, Colorado, *Science*, *191*, 1230–1237, 1976.

Schoenball, M., and W. L. Ellsworth, Waveform relocated earthquake catalog for Oklahoma and Southern Kansas illuminates the regional fault network, *Seismological Research Letters*, *88*, 1252–1258, 2017.

Schoenball, M., N. C. Davatzes, and J. M. G. Glen, Differentiating induced and natural seismicity using space-time-magnitude statistics applied to the Coso Geothermal field, *Geophysical Research Letters*, *42*, 6221–6228, 2015.

Scuderi, M. M., and C. Collettini, The role of fluid pressure in induced vs. triggered seismicity: insights from rock deformation experiments on carbonates., *Scientific reports*, *6*, 24,852, 2016.

Sedgwick, S. M., and S. Mitra, Oil and Gas in California: The Industry and its Economic Contribution in 2015, *Institute of Applied Economics, Los Angeles County Economic Development Corporation*, 2017.

Segall, P., and S. Lu, Injection-induced seismicity: Poroelastic and earthquake nucleation effects, *Journal of Geophysical Research: Solid Earth*, *120*, 1–22, 2015.

Shapiro, S. A., E. Huenges, and G. Borm, Estimating the crust permeability from fluid-injection-induced seismic emission at the KTB site, *Geophys. J. Int.*, *131*, F15—-F18, 1997.

Shapiro, S. A., J. Kummerow, C. Dinske, G. Asch, E. Rothert, J. Erzinger, H. J. Kümpel, and R. Kind, Fluid induced seismicity guided by a continental fault: Injection experiment of 2004/2005 at the German Deep Drilling Site (KTB), *Geophysical Research Letters*, *33*, 2–5, 2006.

Shapiro, S. A., O. S. Krüger, C. Dinske, and C. Langenbruch, Magnitudes of induced earthquakes and geometric scales of fluid-stimulated rock volumes, *Geophysics*, *76*, WC55—-WC63, 2011.

Shirzaei, M., A Wavelet-Based Multitemporal DInSAR Algorithm for Monitoring Ground Surface Motion, *IEEE Geoscience and Remote Sensing Letters*, *10*, 456–460, 2013.

Shirzaei, M., W. L. Ellsworth, K. F. Tiampo, P. J. Gonzalez, and M. Manga, Surface uplift and time-dependent seismic hazard due to fluid injection in eastern Texas, *Science*, *353*, 1416–1419, 2016.

Shirzaei, M., R. Bürgmann, and E. J. Fielding, Applicability of Sentinel-1 Terrain Observation by Progressive Scans multitemporal interferometry for monitoring slow ground motions in the San Francisco Bay Area, *Geophysical Research Letters*, *44*, 2733–2742, 2017.

Skoumal, R. J., M. R. Brudzinski, B. S. Currie, and J. Levy, Optimizing multi-station earthquake template matching through re-examination of the Youngstown, Ohio, sequence, *Earth and Planetary Science Letters*, *405*, 274–280, 2014.

Skoumal, R. J., M. R. Brudzinski, and B. S. Currie, Proximity of Precambrian basement affects the likelihood of induced seismicity in the Appalachian, Illinois, and Williston Basins, central and eastern United States, *Geosphere*, *14*, 1365–1379, 2018.

Skoumal, R. J., A. J. Barbour, M. R. Brudzinski, T. Langenkamp, and J. O. Kaven, Induced Seismicity in the Delaware Basin, Texas, *Journal of Geophysical Research: Solid Earth*, *125*, 1–17, 2020.

Sumy, D. F., E. S. Cochran, K. M. Keranen, M. Wei, and G. A. Abers, Observations of static Coulomb stress triggering of the November 2011 M 5.7 Oklahoma earthquake sequence, *Journal of Geophysical Research: Solid Earth*, *119*, 1904–1923, 2014.

Teng, T. L., C. R. Real, and T. L. Henyey, Microearthquakes and water flooding in Los Angeles, *Bull. Seism. Soc. Am.*, *63*, 859–875, 1973.

Toppozada, T. R., D. M. Branum, M. Reichele, and C. Hallstrom, San Andreas Fault Zone, California: M $>=$5.5 Earthquake History, *Bulletin of the Seismological Society of America*, *92*, 2555–2601, 2002.

Trugman, D. T., and P. M. Shearer, GrowClust: A Hierarchical Clustering Algorithm for Relative Earthquake Relocation, with Application to the Spanish Springs and Sheldon, Nevada, Earthquake Sequences, *Seismological Research Letters*, *88*, 379–391, 2017.

van der Elst, N. J., M. T. Page, D. A. Weiser, T. H. Goebel, S. M. Hosseini, N. J. VanDerElst, M. T. Page, D. A. Weiser, T. H. Goebel, and S. M. Hosseini, Induced earthquake magnitudes are as large as (statistically) expected, *Journal of Geophysical Research*, *121*, 4575–4590, 2016.

Waldhauser, F., W. L. Ellsworth, D. P. Schaff, and A. Cole, Streaks, multiplets, and holes: High-resolution spatio-temporal behavior of Parkfield seismicity, *Geophysical Research Letters*, *31*, L18,608, 2004.

Wang, H., *Theory of linear poroelasticity with applications to geomechanics and hydrogeology*, Princeton University Press, 2000.

Weingarten, M., S. Ge, J. W. Godt, B. A. Bekins, and J. L. Rubinstein, High-rate injection is associated with the increase in U.S. mid-continent seismicity, *Science*, *348*, 2015.

Yeck, W. L., G. P. Hayes, D. E. McNamara, J. L. Rubinstein, W. D. Barnhart, P. S. Earle, and H. M. Benz, Oklahoma experiences largest earthquake during ongoing regional wastewater injection hazard mitigation efforts, *Geophysical Research Letters*, *44*, 711–717, 2017.

Zaliapin, I., and Y. Ben-Zion, Earthquake clusters in southern California I: Identification and stability, *Journal of Geophysical Research: Solid Earth*, *118*, 2847–2864, 2013.

Zaliapin, I., and Y. Ben-Zion, Discriminating Characteristics of Tectonic and Human-Induced Seismicity, *Bullet. Seismol. Soc. Am.*, *106*, 1–14, 2016.

Zhai, G., M. Shirzaei, M. Manga, and X. Chen, Pore-pressure diffusion, enhanced by poroelastic stresses, controls induced seismicity in Oklahoma, *Proceedings of the National Academy of Sciences*, *116*, 16,228–16,233, 2019.

Zhang, Y., M. Person, J. Rupp, K. Ellett, M. A. Celia, C. W. Gable, B. Bowen, J. Evans, K. Bandilla, P. Mozley, and Others, Hydrogeologic controls on induced seismicity in crystalline basement rocks due to fluid injection into basal reservoirs, *Groundwater*, *51*, 525–538, 2013.

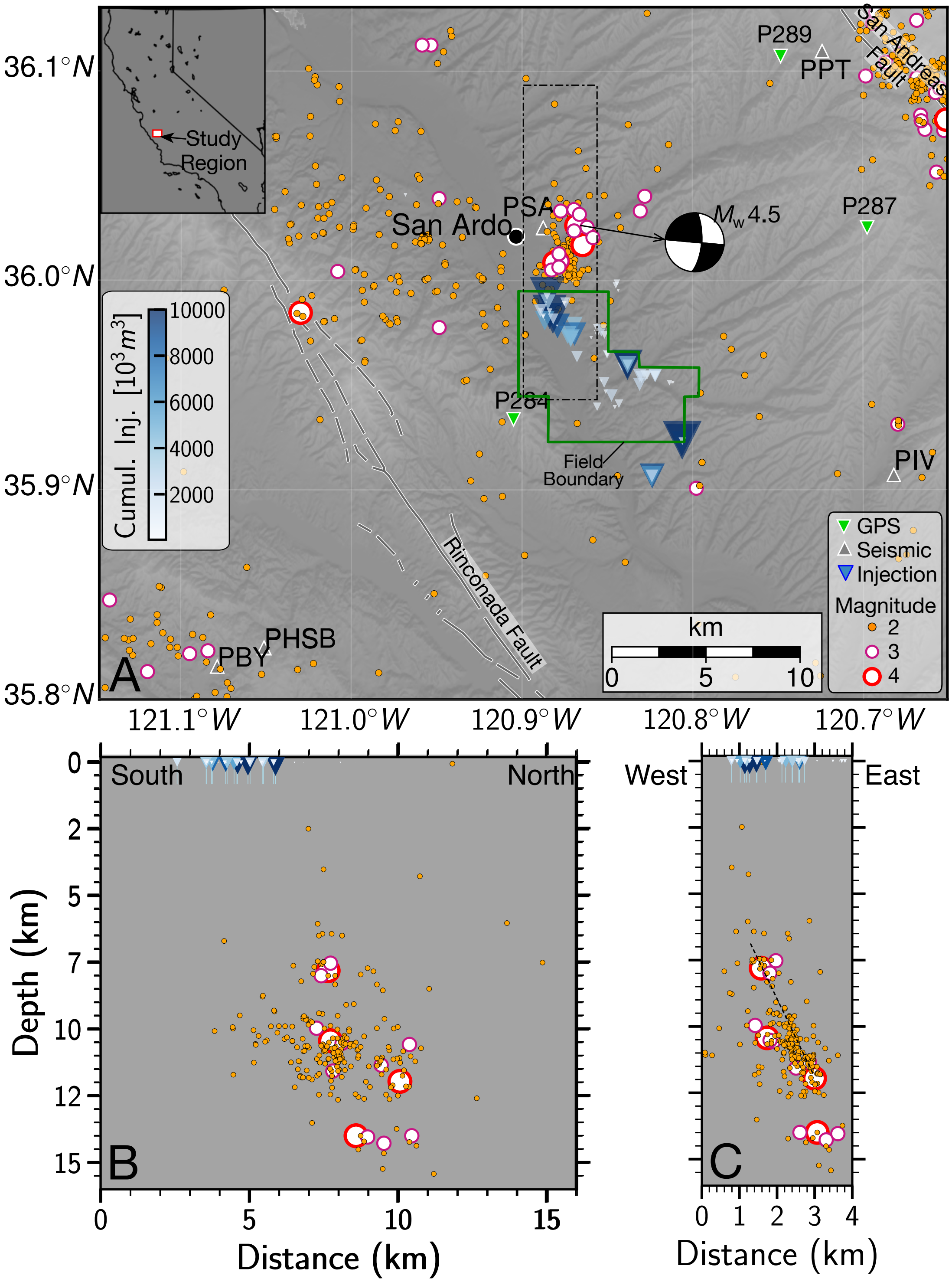

Figure 1: Seismicity and injection wells close to San Ardo after 1970. A: Map of earthquake locations (colored circles, see legend), focal mechanism of the 1985 M_w4.5 event (indicating right-lateral slip on a N-S striking fault), San Ardo oil-field boundary (green polygon), injection well locations (blue triangles, see color bar for injection volumes), GPS stations (green triangles) and seismic stations (gray triangles). The Rinconada and San Andreas faults are labeled to the south-west and north-east of San Ardo. B & C: Depth cross-sections of the seismicity north of the oilfield (dashed rectangle in A). The black dashed line in C highlights the dip of the M_w4.5 event. (see also S1)

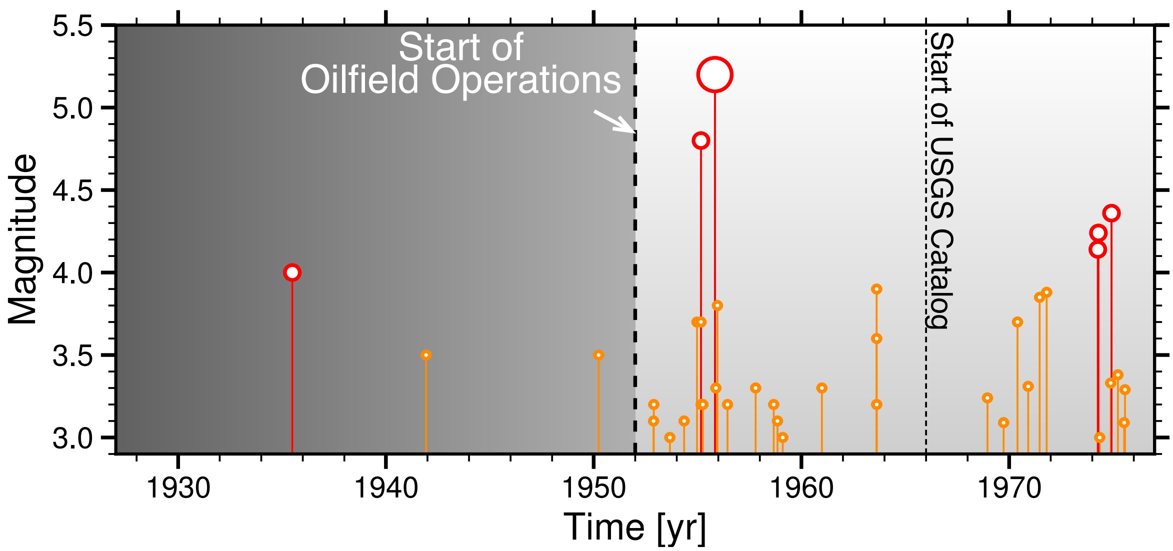

Figure 2: Earthquake activity within 12 km of San Ardo between 1930 and 1978. Larger scale oil-field operations started ∼1952 followed by a slight uptick in seismic activity. The historic seismicity catalog does not suggest temporal main/aftershock clustering.

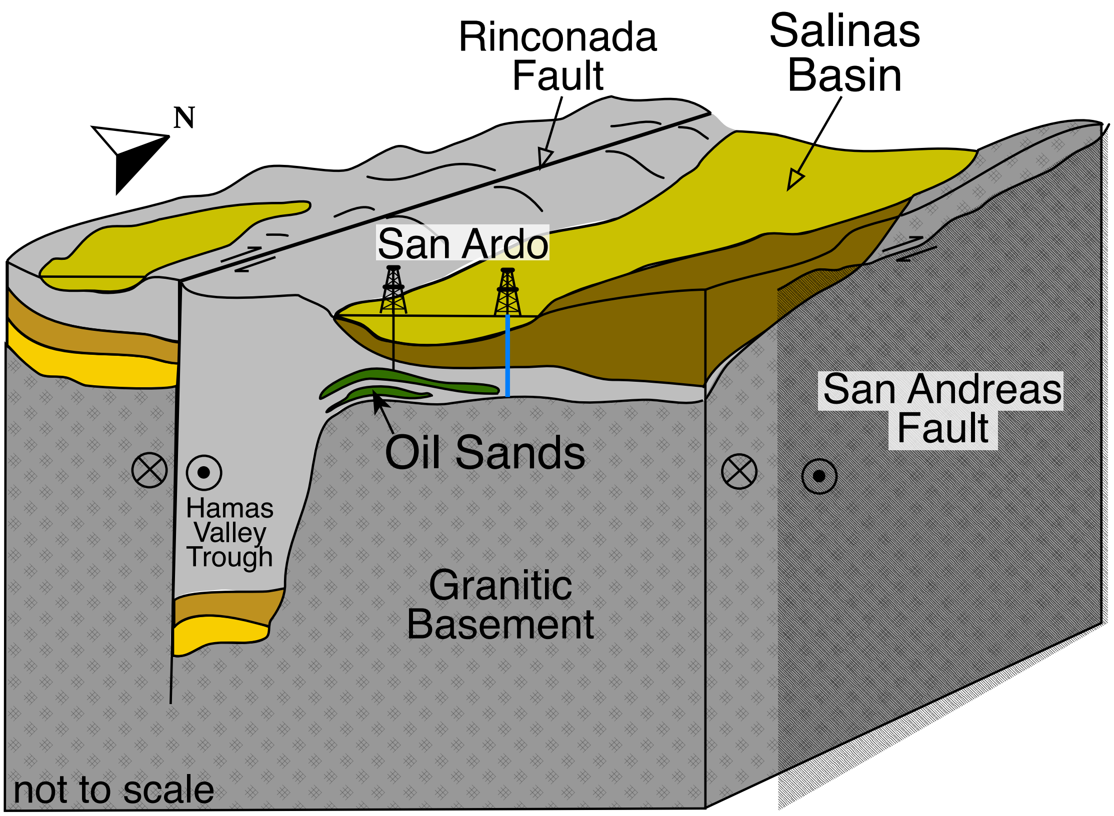

Figure 3: Geologic setting at the southern end of Salinas basin for a west-east transect through the San Ardo oilfield. Oil-bearing sands are highlighted in green, granitic basement in dark gray and shallow sedimentary layers in light gray, yellow and brown colors. (modified from *Menotti*, 2014). Fluid injection occurs right above the granitic basement in the northern part of the oilfield.

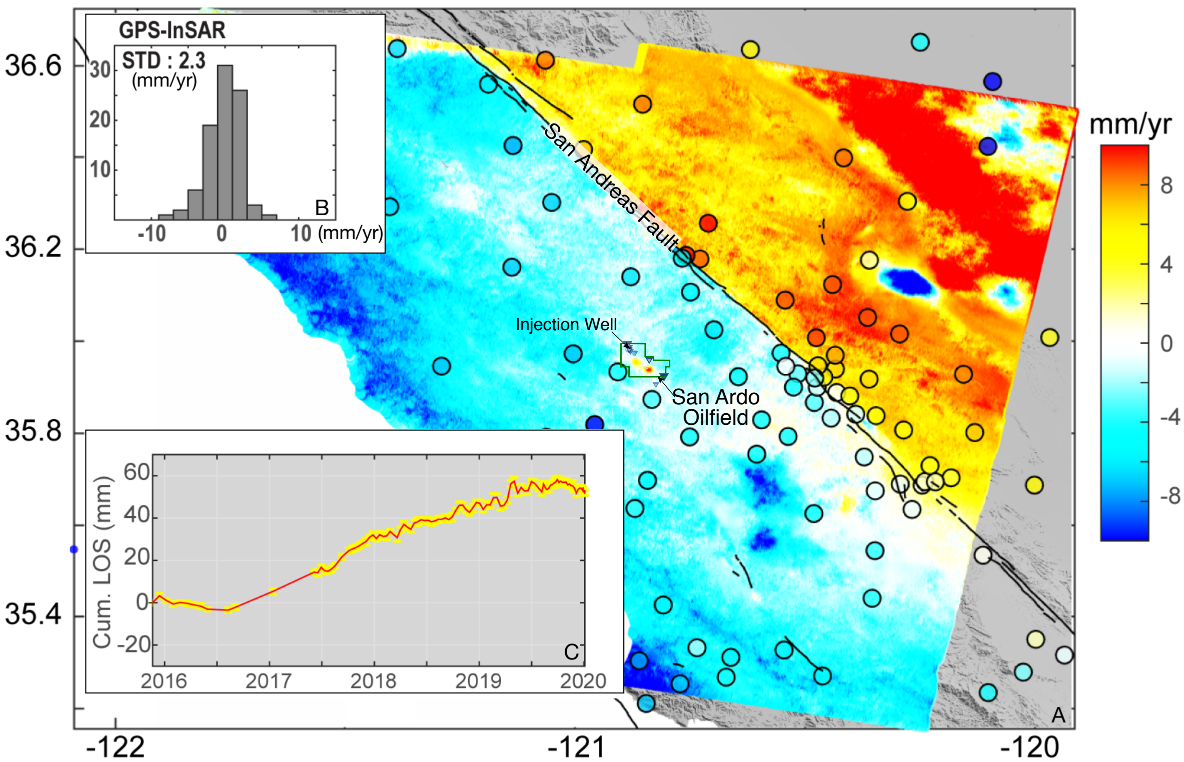

Figure 4: Line-of-sight (LOS) velocities and displacements associated with injection activity in San Ardo. A: InSAR results (see legend) and local GPS measurements (black circles) with 3D displacement projected onto the line-of-site direction of the imaging satellite. The velocity map is dominated by the left-lateral shearing along the San Andreas Fault. The San Ardo oilfield exhibits the strongest positive LOS velocity west of the San Andreas fault. (see Fig. S6 for a close up) B: The histogram shows the differences between InSAR and GPS with a standard deviation of 2 mm/yr. C: InSAR displacement time series toward the center of the oilfield between 2016 and 2020. The yellow envelope indicates the 1-sigma error range.

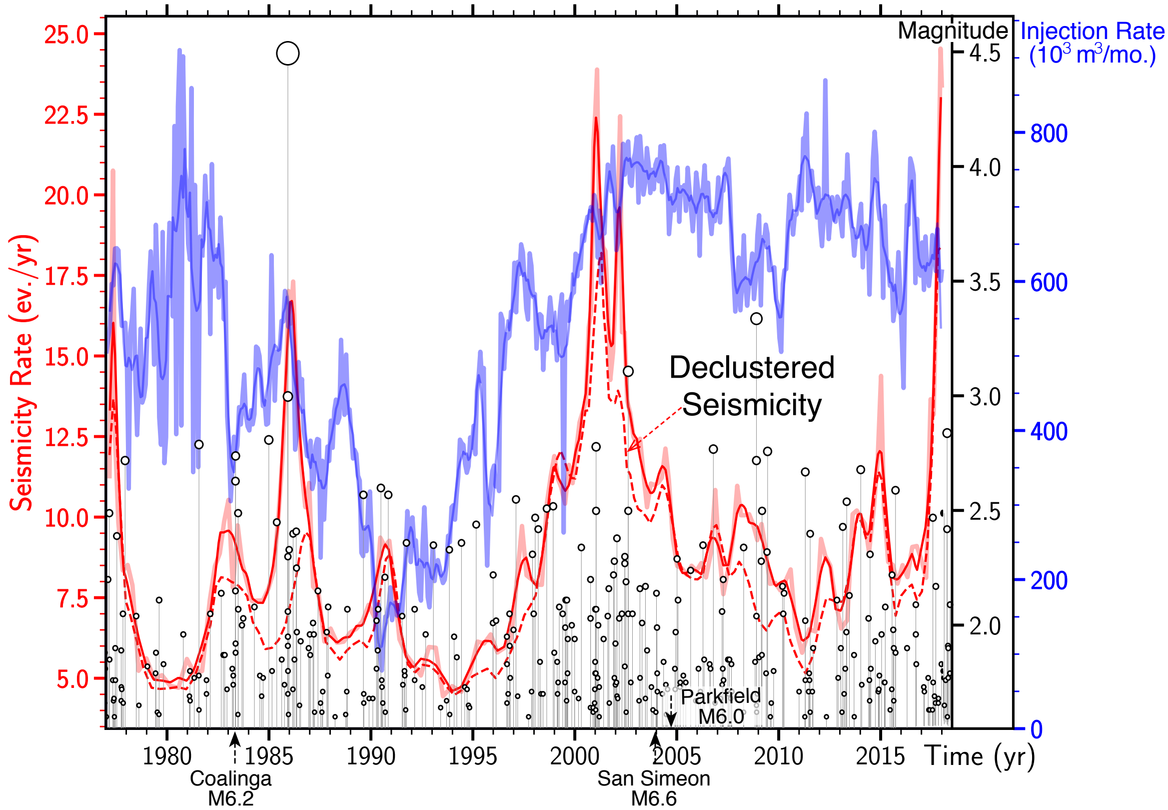

Figure 5: Seismicity (red curve) and fluid injection (blue curve) rates within 20 km of the San Ardo oilfield between 1975 and 2019. Event magnitudes are shown by black circles and declustered seismicity rates are highlighted by a dashed red line. Seismicity rates are determined for events above the magnitude of completeness (M_c=1.6). The largest events during this period are a M4.5 earthquake in 1985 and a M3.3 event in 2008.

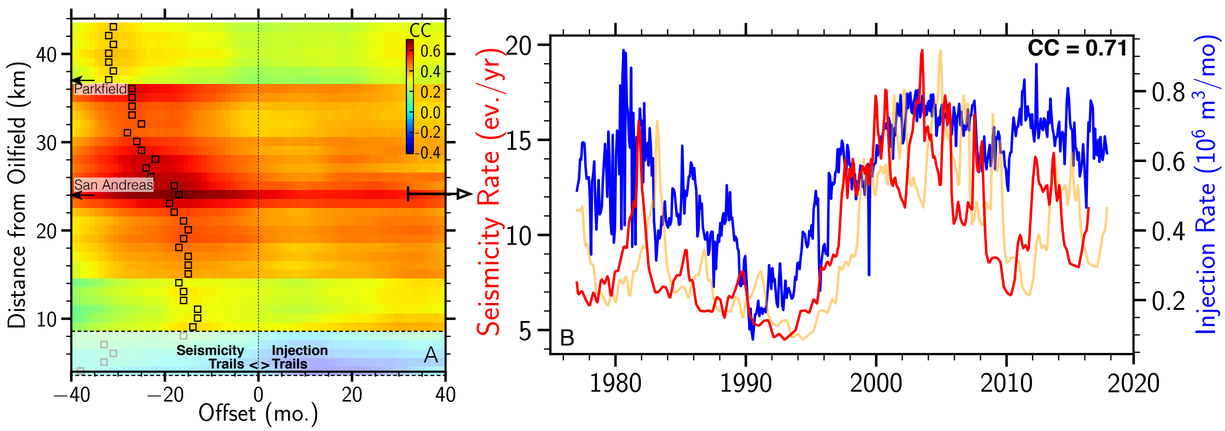

Figure 6: Left: Cross-correlation coefficients (see color bar) for injection and seismic events at increasing radii from the oil-field (y-axis) as a function of lag-time (x-axis). Correlation coefficients increase gradually for larger seismic records out to 24 km at which the San Andreas fault is located. At larger distances, correlations decrease due to the inclusion of San Andreas fault and Parkfield events. Cross-correlation results are significant at distances beyond 8 km. Right: Seismicity (red) and injection (blue) rates for events within 24 km from San Ardo. Orange curve shows original seismicity rates and the red curve shows shifted rates that maximize the cross-correlation coefficient (CC=0.71).

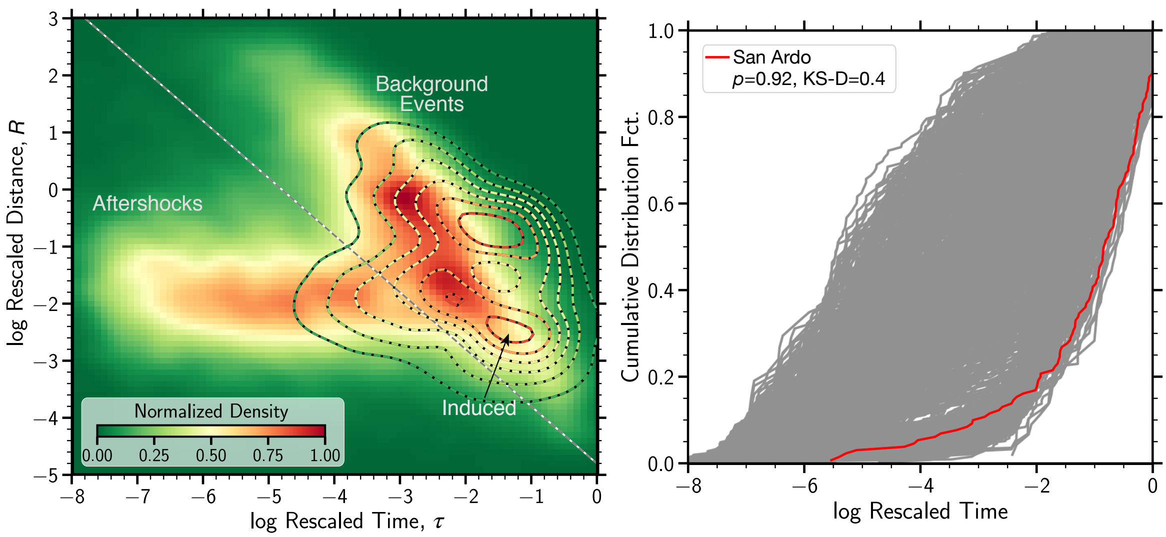

Figure 7: Left: Rescaled distance and time for nearest-neighbor event pairs for the entire Northern California earthquake catalog (color map) and solely for San Ardo seismicity (contours). The NC catalog shows two dominant statistical modes associated with clustered events at small inter-event times and distances and a background mode at large distances and times. These two modes are separable by comparison with randomized catalogs (gray dashed line). The San Ardo seismicity exhibits a third mode at close distances which is characteristic for induced events (*Zaliapin and Ben-Zion*, 2016). Right: Conditional inter-event time distributions at small distances ($\log R \leq -2.5$) for Monte Carlo resampled catalogs (gray) and observed distributions in San Ardo. The San Ardo seismicity falls within the 92^{nd} percentile of the overall catalog variability at small R.

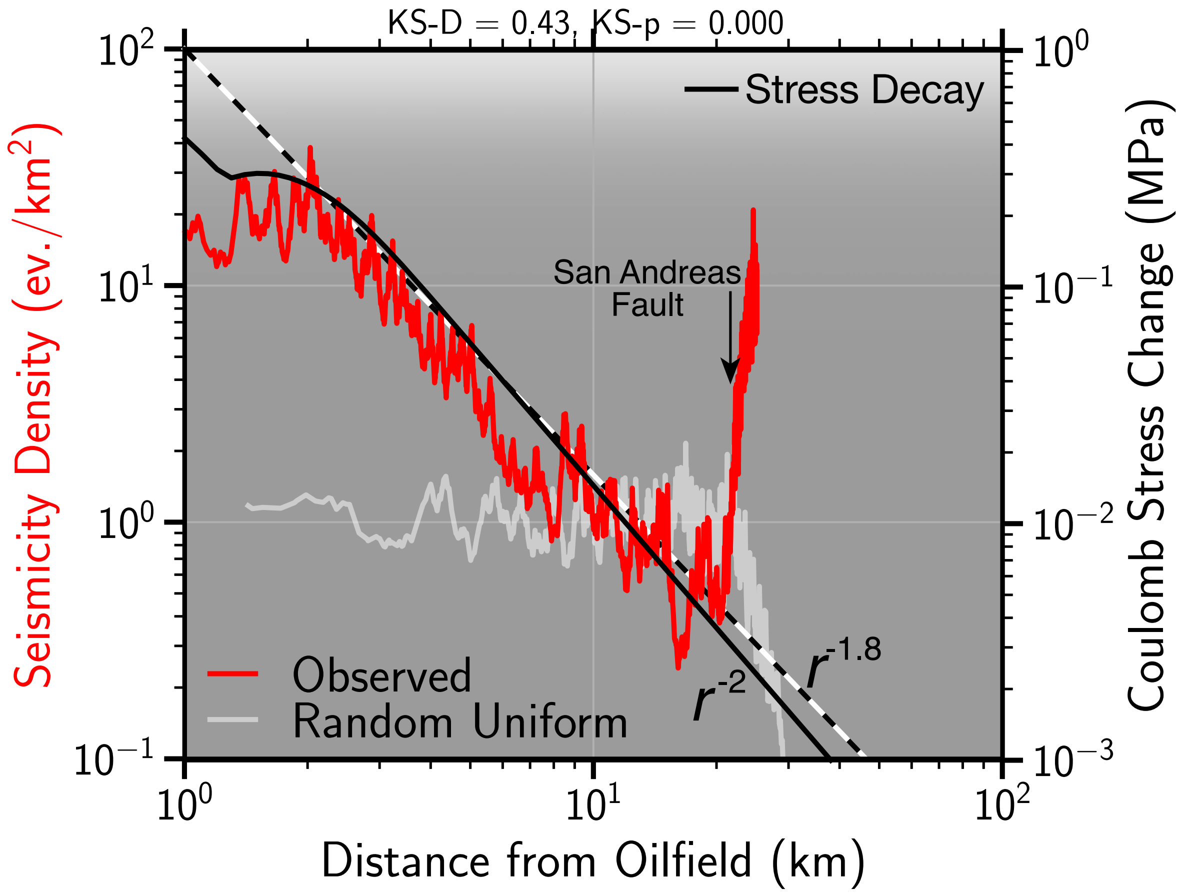

Figure 8: Seismicity density decay (red) as a function of surface distance from the San Ardo oilfield, compared to spatially uniform seismicity (gray). The spatial decay is roughly in agreement with observed power-law decay of earthquakes from single injectors which decay as $r^{-1.8}$ (white dashed line) (*Goebel and Brodsky*, 2018). The black line shows the stress decay from an analytical poroelastic model of fluid injection in a vertically confined reservoir with spatial decay of r^{-2}. Seismicity density increases rapidly at the distance of the San Andreas fault.

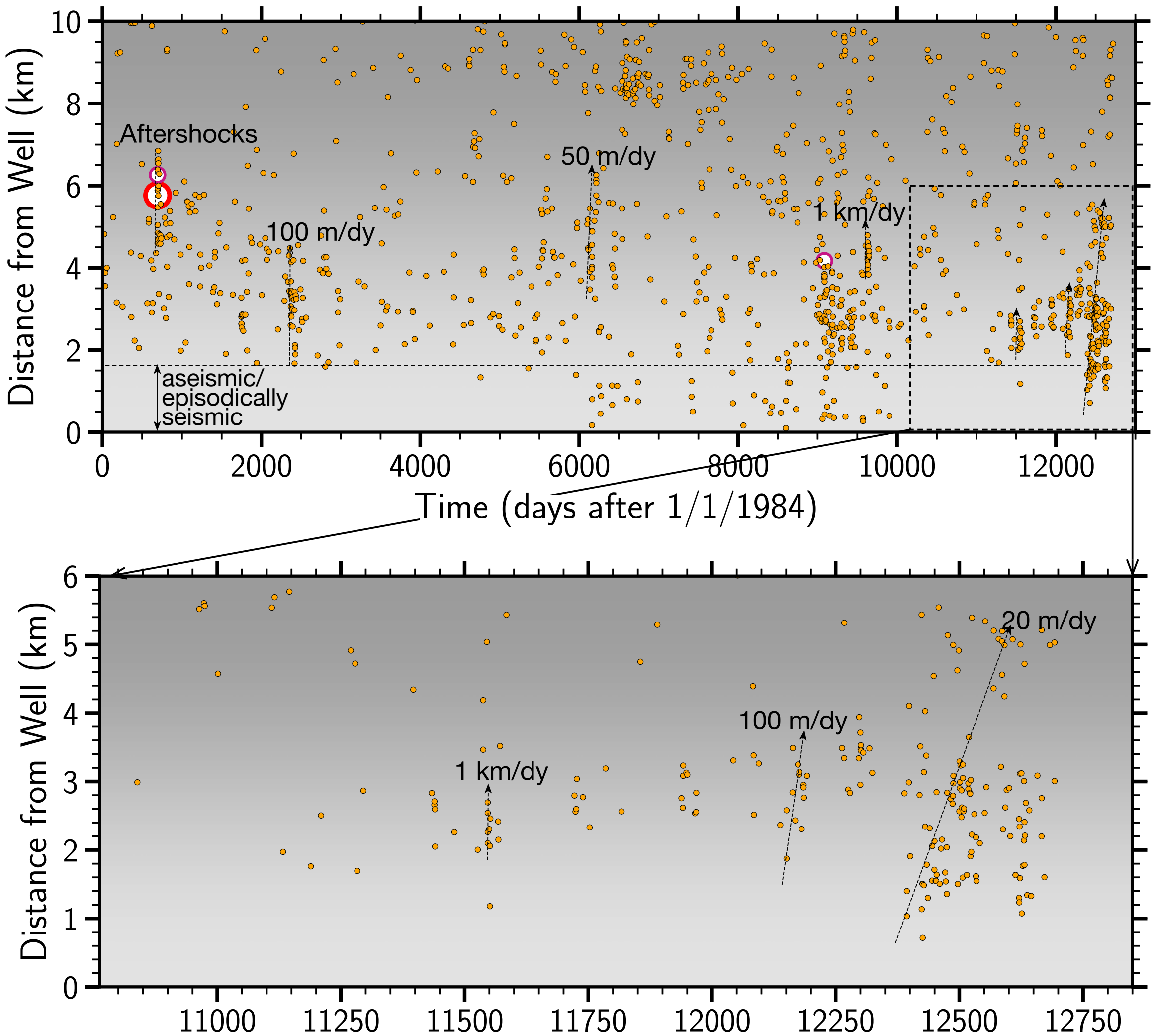

Figure 9: Seismicity within 10 km from the San Ardo oilfield between 1984 and 2018. Earthquakes are colored according to magnitude (orange: $M<3$, magenta: $M3$, red: $M4$). The immediate zone within 1 to 2 km from the injection wells is predominantly aseismic. Seismicity clusters that indicate linear migration are highlighted by black arrows. Migration speeds may range from 0.02 to 1.0 km/dy.

Supplementary Material: More than 40 years of potentially induced seismicity close to the San Andreas fault in San Ardo, central California

Thomas H. W. Goebel
Center for Earthquake Research and Information
University of Memphis, Tennessee, USA
thgoebel@memphis.edu

Manoochehr Shirzaei
Department of Geoscience
Virginia Tech, Blacksburg, VA, USA

September 26, 2020

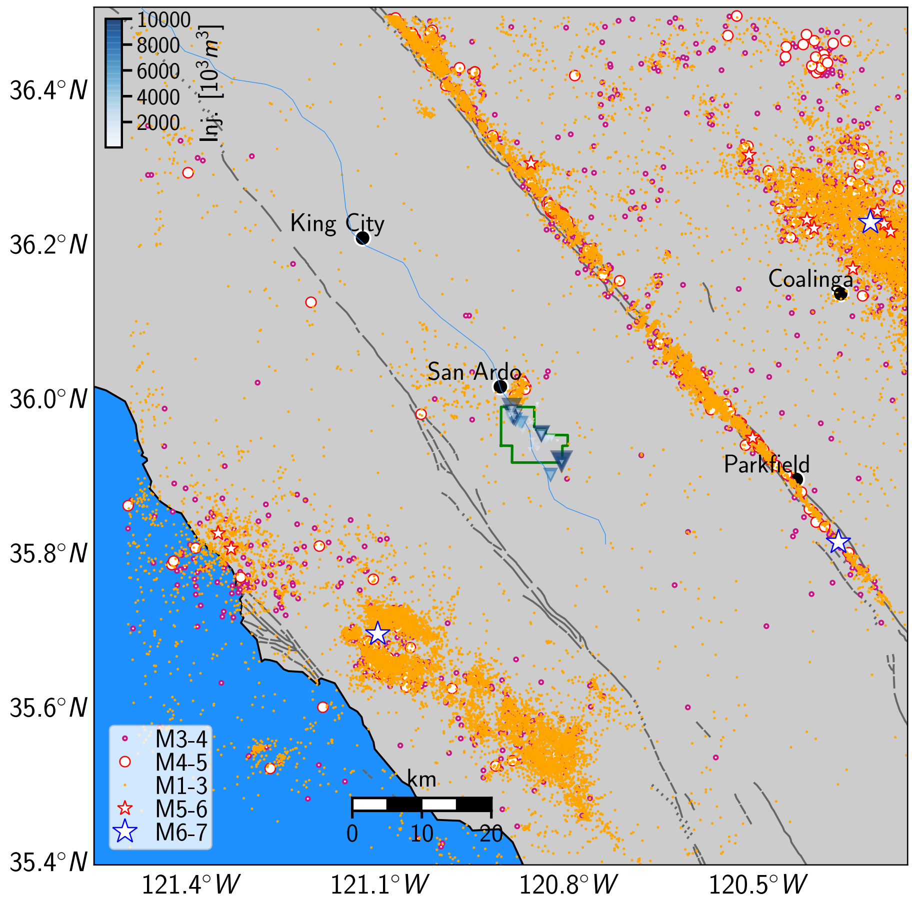

Figure S1: Seismicity, faults and injection well locations within coastal central California. Earthquakes are colored according to size (orange: $M > 3$, magenta: $M3-4$, red circle: $M4-5$, red star: $M5-6$, blue star: $M \geq 6$). The largest events from North to South are the 1983 Coalinga, the 2004 Parkfield and the 2003 San Simeon events. Waste water disposal wells are shown by blue triangles and the San Ardo oilfield is highlighted by a green polygon.

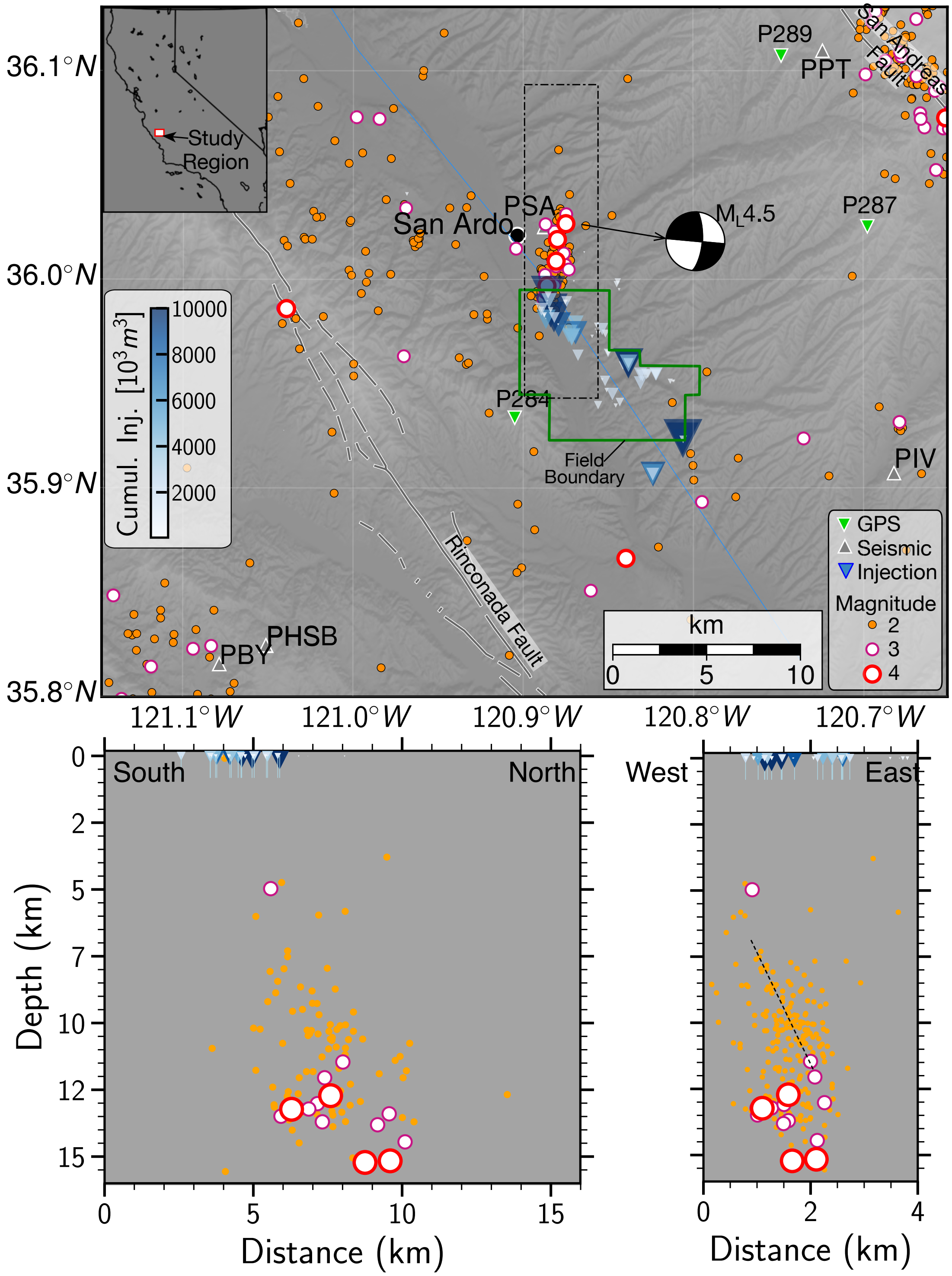

Figure S2: Same as Figure 1 in the main text but for seismicity from the combined historic Berkeley and NCEDC catalogs from 1930 to 2020.

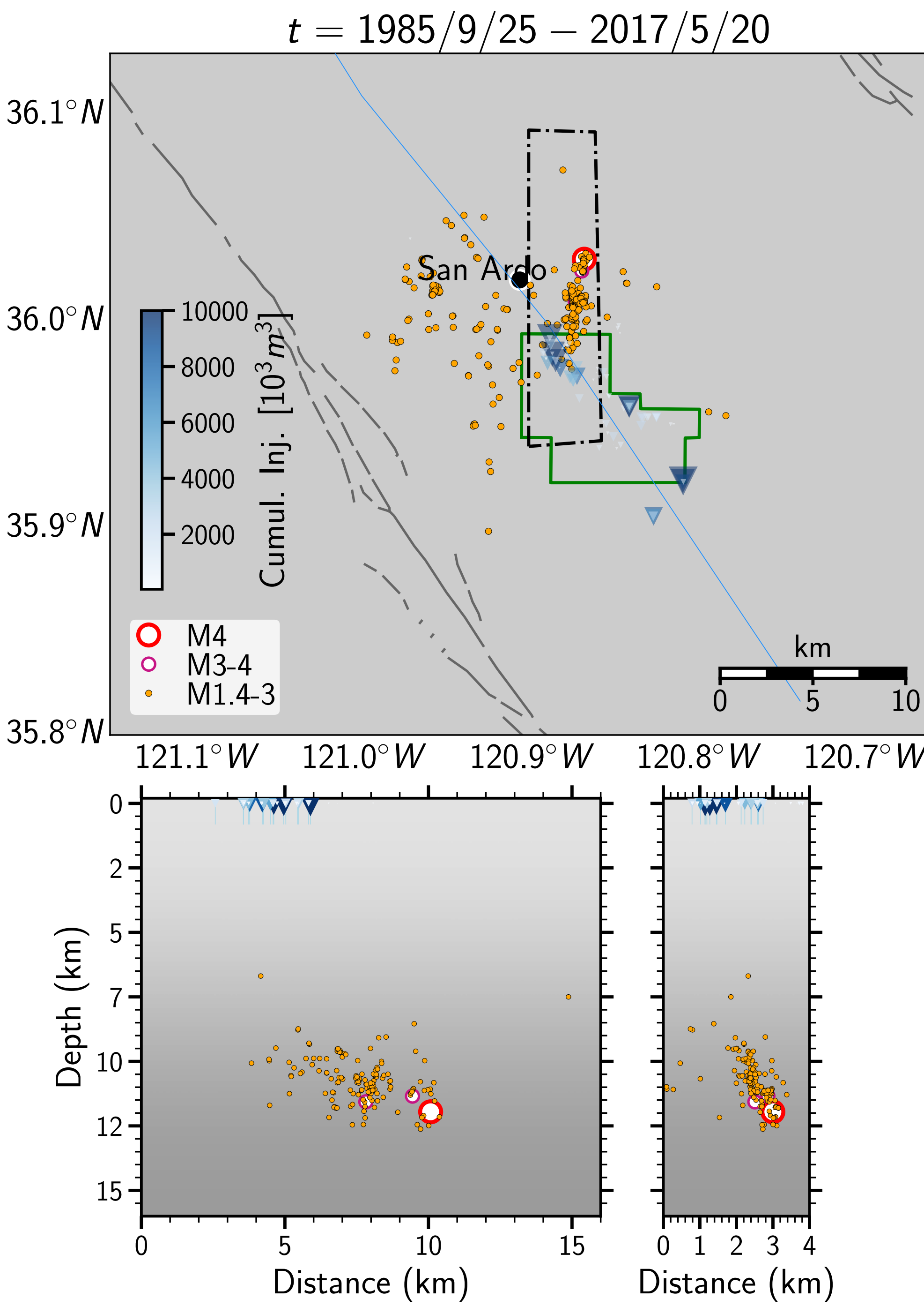

Figure S3: Same as Figure S2 but only for events relocated with GrowClust

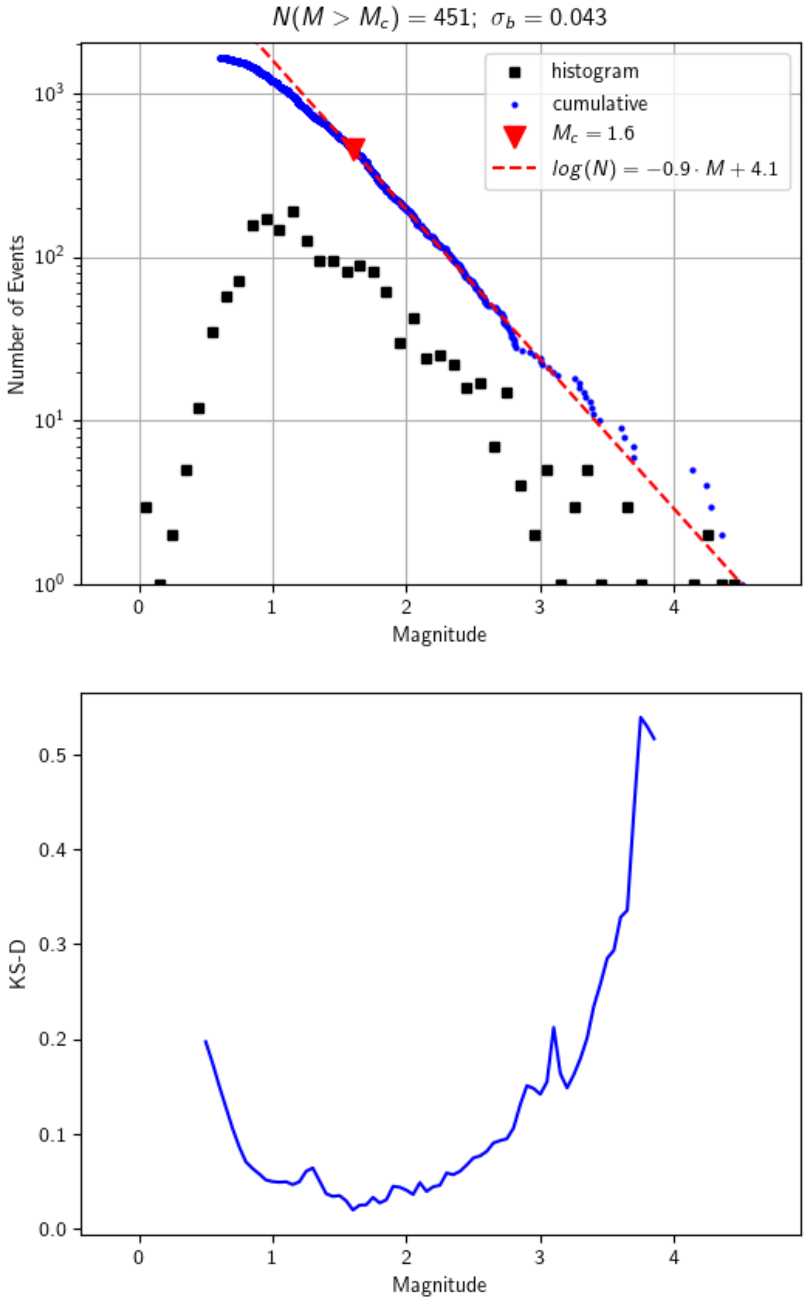

Figure S4: Top: Frequency-magnitude distribution, b-value and magnitude of completeness, M_c, for the San Ardo seismicity. Bottom: Misfit function between observed and modeled distribution, which was used to determine M_c.

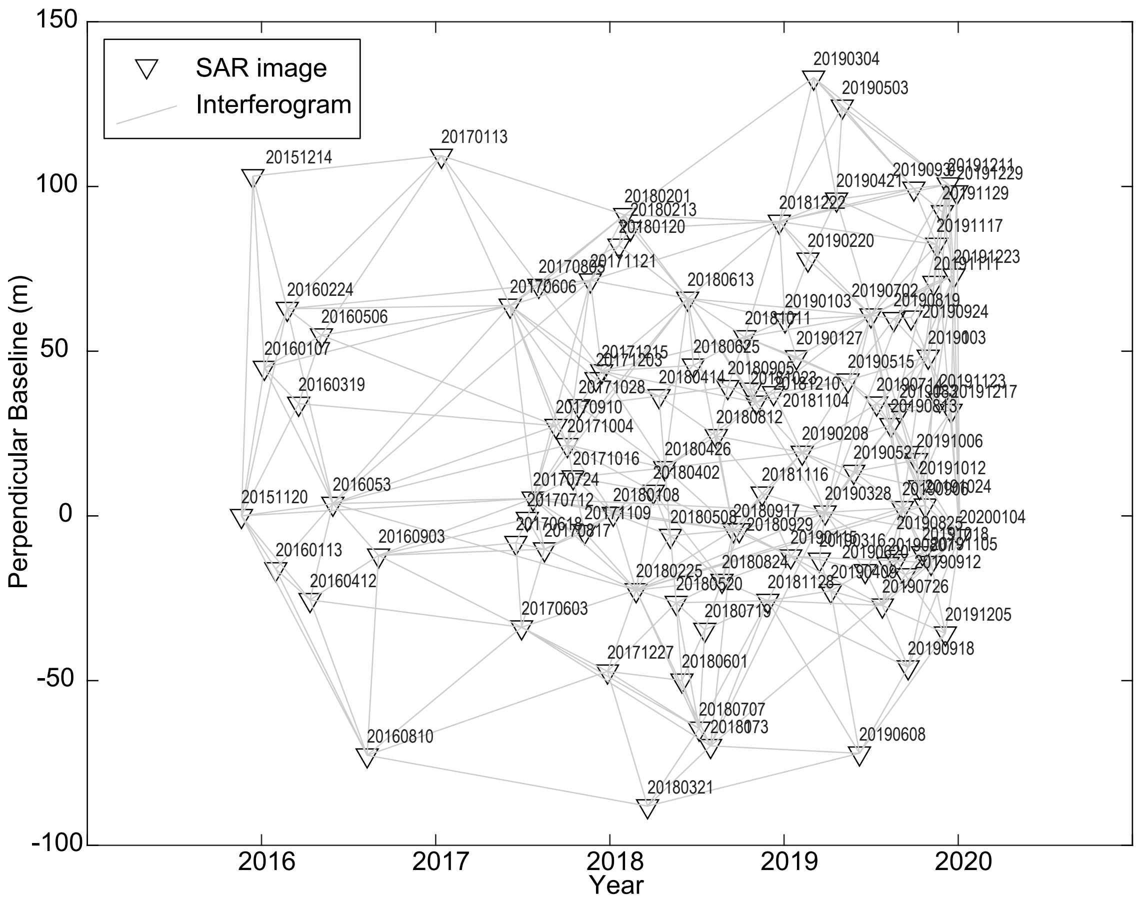

Figure S5: Baseline plot showing the temporal and perpendicular baseline of the interferometric dataset used for generating surface deformation map over the San Ardo injection site.

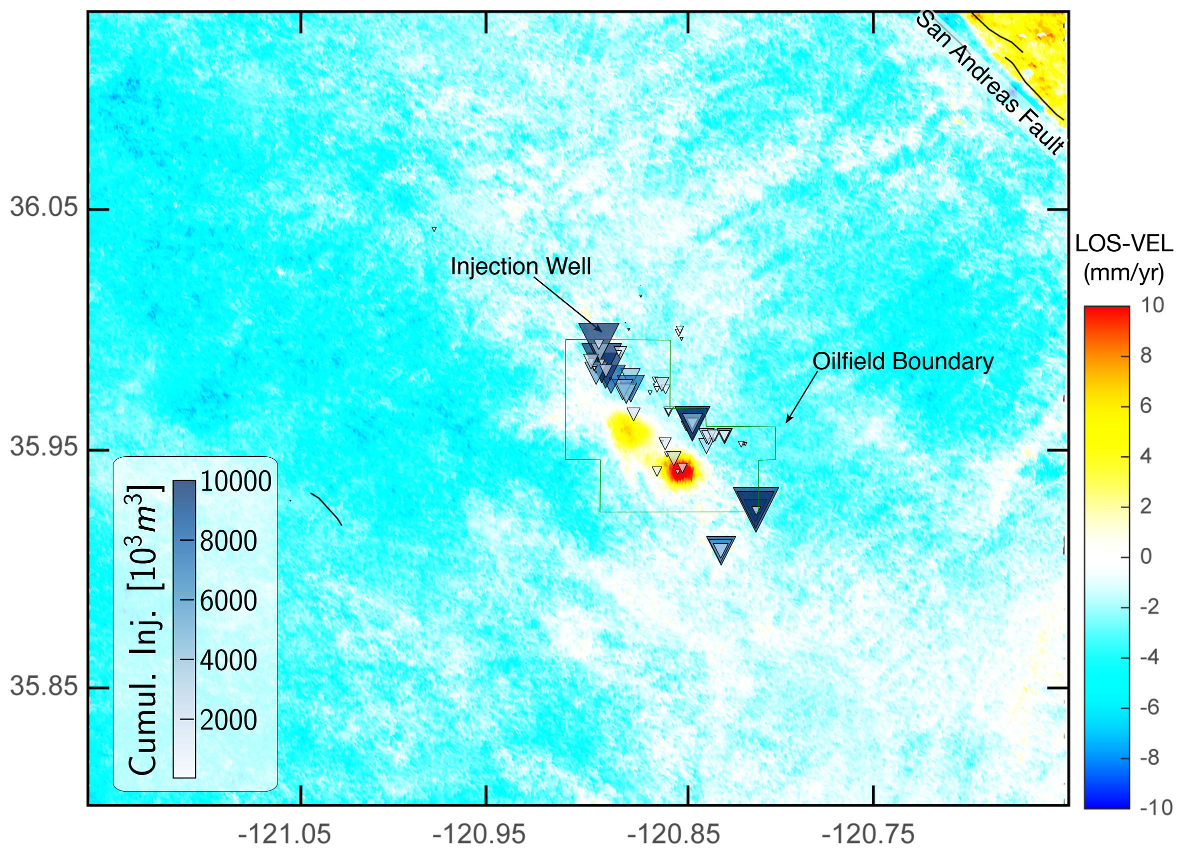

Figure S6: Same as Figure 4 in the main text but zoomed into the San Ardo area to highlight the local surface uplift above the oilfield. The spatial distribution of the LOS velocity was obtained from multi-temporal InSAR processing of Sentinel-1A/B data sets.

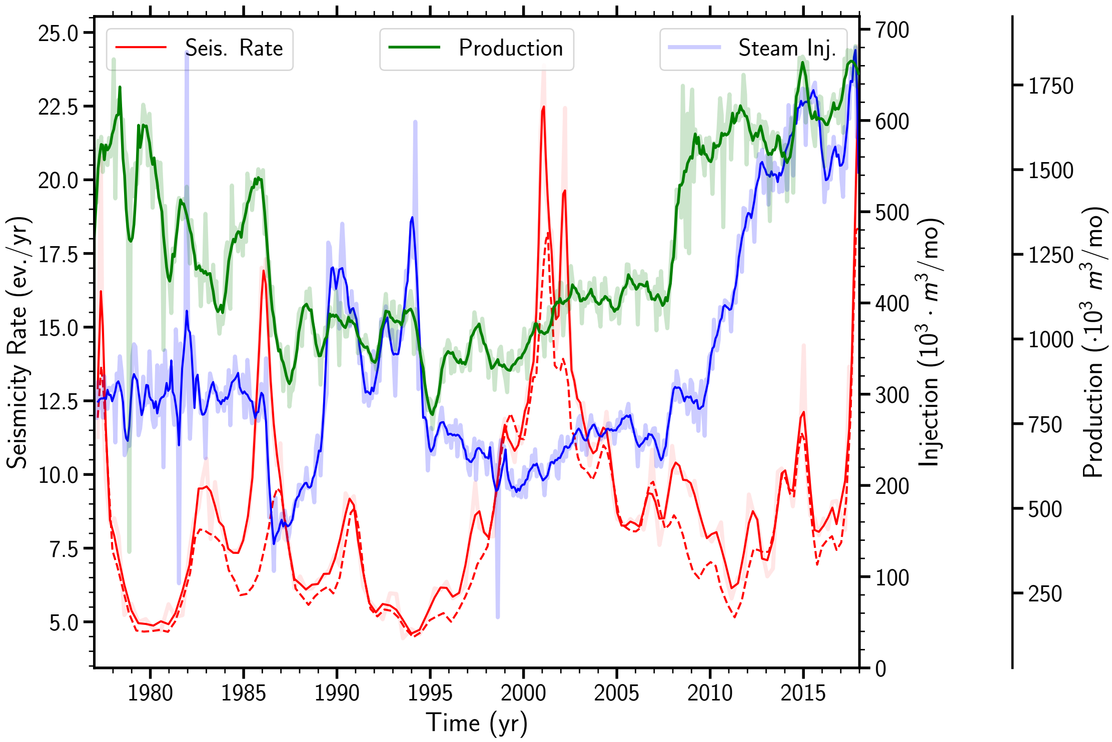

Figure S7: Seismicity (red), production (green) and steam injection (blue) for the San Ardo oilfield between 1977 and 2018. This figure highlights that correlations between other operational parameters and seismicity are not very pronounced. (compare with Fig. 5 in the main text).